Moon-based EUV imaging of the Earth's Plasmasphere: Model simulations

Fei He,[1] Xiao-Xin Zhang,[2] Bo Chen,[1] Mei-Ching Fok,[3] and Yong-Liao Zou[4]

[1]   The EUV imager on board the Chang'E-3 lunar lander will image the Earth's plasmasphere from a lunar perspective to focus on some of the open questions in plasmaspheric researches (i.e., global structures, erosion, and refilling of plasmasphere). In order to achieve the understanding of the plasmaspheric dynamics in relation to these EUV images in lunar perspective, the He$^+$ 30.4 nm emission intensities and global structures of the plasmasphere viewed from the moon are investigated using a dynamic global core plasma model embedded with TS07 magnetic field model and W05 electric field model. Two typical storms observed by the IMAGE EUV imager are systematically simulated from the perspectives of the moon. It is found from the simulations that the maximum emission intensity of the plasmasphere is ~12.3 R which is greater than that detected from polar orbit, and the global shapes and temporal evolutions of large-scale plasmaspheric structures (plasmapause, shoulder, and plume) also have different patterns in moon-based simulated images. It is also shown that the plasmaspheric structures extracted from moon-based EUV images are in agreement with those from IMAGE EUV images. Systematic simulations demonstrate that specific latitudinal distribution of the plasmaspheric structures can only be imaged at specific positions in lunar orbit. It is expected that this investigation provides us with an overall understanding on moon-based EUV images and helps to identify the plasmaspheric structures and evolution patterns in future moon-based EUV imaging.

Citation: He, F., X.-X. Zhang, B. Chen, M.-C. Fok, and Y.-L. Zou (2013), Moon-based EUV imaging of the Earth's Plasmasphere: Model simulations, *J. Geophys. Res. Space Physics*, *118*, 7085–7103, doi:10.1002/2013JA018962.

1.   Introduction

[2]   The Earth's plasmasphere located above the ionosphere is a torus of low energy, dense plasma region with ions and electrons all trapped on geomagnetic field lines, forming a cold thermal plasma cloud up to $5 \sim 6\ R_E$ (Earth radii). The plasmaspheric He$^+$ ions resonantly scatter the extreme ultraviolet (EUV) radiation of sunlight at 30.4 nm with intensity proportional to the column density along a line of sight (LOS) [*Meier and Weller*, 1972; *Meier*, 1991]. Since He$^+$ ion is the second abundant component in the plasmasphere [*Craven et al.*, 1997], the 30.4 nm emission is a natural choice for imaging the global plasmasphere given that H$^+$ has no optical emission. In addition, the magnetosphere is optically thin to this emission [*Brandt*, 1961], and the interplanetary radiation background intensity at 30.4 nm is extremely low [*Paresce et al.*, 1981; *Gruntman*, 1992; *Jelinsky et al.*, 1995]. Thus, the He$^+$ 30.4 nm emission can be used to image the global plasmasphere, and the EUV images are intuitively suitable for researches on the dynamics and global structures of the plasmasphere during storms/substorms, as well as for space weather monitoring and forecasting.

[3]   The most significant progress in remote sensing of the plasmasphere in the past decades is the application of the wide field of view (FOV) optical cameras that image the plasma by detecting the resonantly scattered 30.4 nm sunlight from the He$^+$ in the plasmasphere [*Carpenter*, 2004]. The X-ray ultraviolet (XUV) scanner on board the Planet-B mission [*Nakamura et al.*, 1999] carried out scanning imaging of the 30.4 nm emission of the plasmasphere during its travel to the Mars and for the first time obtained the partial plasmaspheric He$^+$ emission intensity distribution projected on the meridian plane [*Nakamura et al.*, 2000]. The first comprehensive EUV imaging of the plasmasphere was carried out by the EUV imager on board the IMAGE spacecraft in the apogean region of polar orbit [*Burch*, 2000; *Sandel et al.*, 2000]. Many important features of the plasmasphere were observed [*Sandel et al.*, 2001, 2003; *Adrian et al.*, 2001; *Goldstein et al.*, 2002; *Gallagher et al.*, 2005]. The telescope of extreme ultraviolet (TEX) on board the Selenological and Engineering Explorer (SELENE) (also known as KAGUYA) mission [*Sasaki et al.*, 2003] conducted overall imaging of the plasmasphere from lunar polar orbit [*Yoshikawa et al.*, 2008].

---

[1]Changchun Institute of Optics, Fine Mechanics and Physics, Chinese Academy of Sciences, Changchun, China.
[2]National Center for Space Weather, China Meteorological Administration, Beijing, China.
[3]NASA Goddard Space Flight Center, Greenbelt, Maryland, USA.
[4]National Astronomical Observatories, Chinese Academy of Sciences, Beijing, China.

Corresponding author: X.-X. Zhang, National Center for Space Weather, China Meteorological Administration, Beijing 100081, China. (xxzhang@cma.gov.cn)

However, the XUV only imaged the partial plasmasphere during its near-Earth parking orbit from July 1998 to January 1999 because of its limited operation period and FOV of scanner; the EUV imager is mounted on a spin platform, and the IMAGE mission is operated in polar orbit with limitations of FOV and different vantage points, and only half (or less) of the duty circle is looking at the Earth; therefore, the plasmasphere cannot be imaged continuously, and the TEX was mounted on a three-axis stabilized platform, and the SELENE mission was operated in lunar polar orbit, and more than half of its duty circle was at the back of the moon; therefore, the plasmaspheric evolution during geomagnetic storms/substorms might not be completely imaged.

[4] These problems might be eliminated in the moon-based EUV imaging. The equivalence of the spin period and the revolution period of the moon makes its one side always face the Earth. If an EUV imager is set on the surface of the moon facing the Earth, the FOV of the imager will always point to the Earth. Although there are small longitudinal and latitudinal disturbances due to the elliptic orbit of the moon and due to the angle (5.15°) between the plane of the lunar orbit and the ecliptic [He et al., 2010a], these disturbances can be compensated by daily rotation of the imager. Thus, the imager will image the plasmasphere continuously during lunar revolution circling the Earth except for the full moon when the sunlight will go into the imager directly (the imager must be shut down). The distance of ~60 R_E from the Earth to the moon makes the FOV of the imager relatively small and easy to be achieved, and the uniform spatial resolution can be realized in the whole FOV at the same time. It is worthwhile to note that this long distance leads to increased integration time and/or decreased effective imaging area due to the r^{-2} decrease of the photon flux per unit area for the moon-based EUV imaging.

[5] In the second phase of Chinese Lunar Exploration Program, which will be implemented in 2013, an EUV imager with FOV of 15°, angular resolution of 0.095°, temporal resolution (or integration time) of 10 min, and sensitivity of 0.12 count $R^{-1} s^{-1}$ pixel^{-1} will be mounted outside the instrumental module on the top of the lunar lander of the Chang'E-3 (CE-3) mission to image the 30.4 nm emissions resonantly scattered by the Earth's plasmasphere and then to study the dynamics of the plasmasphere from a new perspective. The moon-based EUV imager is able to detect the intensity less than 0.1 R and to recognize various structures of the plasmasphere (e.g., plasmapause, plume, and shoulder). The moon-based EUV images from this mission can be used to answer some open questions in plasmaspheric researches, such as the intensity distributions and the global structures of the plasmasphere, the erosion and refilling processes of the plasmasphere, the plasmaspheric responses to the solar wind and the interplanetary magnetic field (SW-IMF) and geomagnetic disturbances, and the transport of thermal plasma throughout the geospace and the inner magnetosphere.

[6] It is expected that the moon-based EUV imaging will provide us an opportunity to study the plasmasphere from side perspectives. Since the resonantly scattered intensity of 30.4 nm emission is proportional to the column density of He$^+$ along the integration path or LOS, EUV imaging from the moon enables us to study the overall dynamics of the plasmasphere. The moon-based images can also be used to analyze the latitudinal magnetic flux tube dynamics of the plasmasphere,

which is impossible to be obtained from polar perspectives. Furthermore, when the moon-based EUV imager is combined with high polar orbit EUV imagers orbiting the Earth, the "true" three-dimensional (3-D) plasmaspheric density distributions can be obtained by inversing the simultaneous images from the polar orbit and the moon. When the moon-based EUV imager is combined with polar orbit auroral imagers, ionospheric imagers, and energy neutral atoms (ENA) imagers, the coupling dynamics of the plasmasphere to the ionosphere, to the radiation belt, and to the ring current can be comprehensively investigated.

[7] Since no plasmaspheric EUV global images have been currently obtained from the moon (it is noted that the FOV of TEX is just 5° × 10°, which cannot image the overall plasmasphere in one snapshot), it is essential to simulate the moon-based EUV imaging to understand the plasmasphere systematically before the launch of the CE-3 moon-based EUV imager. Swift et al. [1989] simulated the O$^+$ 83.4 nm emissions in the magnetosphere to study the global changes in the magnetospheric plasma and derive the specification of the imaging instrument. Garrido et al. [1994] simulated the He$^+$ 30.4 nm and O$^+$ 83.4 nm emissions in the plasmasphere to reflect their emission intensities and structures in the magnetosphere from the side view but not so far as from the moon. The modeling principles in these two studies are the same, but their spatial resolutions were limited by their density models. In this investigation, the dynamic global core plasma model (DGCPM), which can simulate many fine structures of the plasmasphere [Ober et al., 1997, 1998; Gallagher et al., 2005; Liemohn et al., 2004, 2006; He et al., 2012], is used to study the evolutions of the global structures of the plasmasphere viewed from the moon and to understand how these structures will appear in the moon-based simulated images.

[8] In an earlier work [He et al., 2010b], we have briefly reported the calculation results of the scattering intensity of the plasmasphere from the lunar perspectives for guiding the design of the moon-based EUV imager. In this paper, we will provide a thorough and systematic investigation of the plasmaspheric structures (such as the shoulders and the plumes) and their evolutions from lunar perspectives. The simulation approach including the DGCPM model, the 3-D density construction, and the imaging method will be introduced in section 2. Then, two storms observed by IMAGE EUV will be simulated from the moon in section 3 to investigate the global plasmaspheric images and storm time plasmaspheric evolutions in moon-based EUV imaging, especially the evolution of shoulders and plumes. Finally, discussions and summary will be given in sections 4 and 5, respectively.

2. Simulation Approach

2.1. Model Description

[9] The DGCPM established by Ober et al. [1997] is used to calculate the total ion density (H$^+$, He$^+$, and O$^+$; other ions are neglected) in the plasmasphere, and then, it is transformed to He$^+$ density. The model solves the following continuity equation [Chen and Wolf, 1972; Rasmussen et al., 1993]:

$$\frac{D_\perp N}{Dt} = \frac{F_n}{B_{ni}} + \frac{F_s}{B_{si}} \tag{1}$$

where $D_\perp/Dt$ is the convection derivative in the moving frame ($E \times B$) of the magnetic flux tube, N is the total ion

content per unit magnetic flux tube assuming the density along a magnetic flux tube to be a constant, F_n and F_s are the flux in or out the magnetic flux tube at the northern and southern ionospheres, and B_{ni} and B_{si} are the magnetic field strengths at the northern and southern ionospheric foot points of the magnetic flux tube, respectively. It is noted that B_i in *Ober et al.* [1997] is broken into north/south components to accommodate the output from Tsyganenko field model.

[10] Empirical models of the magnetic field and electric field should be specified in the plasmaspheric region. The magnetic field is specified by the International Geomagnetic Reference Field (IGRF) model and the Tsyganenko model (TS07) [*Tsyganenko and Sitnov*, 2007; *Sitnov et al.*, 2008]. The electric field pattern obtained from Weimer convection model (W05) [*Weimer*, 2005] is mapped into the plasmasphere along magnetic field lines, each of which is assumed to be equipotential.

[11] The numerical results from equation 1 can be used to derive the plasmaspheric density distribution at specified times. The plasmaspheric magnetic flux tubes initialized with saturated density [*Carpenter and Anderson*, 1992] are used to drive the DGCPM model for 5–6 days to reach an equilibrium stage under quiet solar wind conditions, and the model is then switched to strong SW-IMF conditions to simulate the structures and evolutions of plasmasphere during storm times.

2.2. He$^+$ Density Calculation

[12] The He$^+$ density can be derived once the density ratios between He$^+$ and H$^+$ and between O$^+$ and H$^+$ are given, based on that the output of the DGCPM, n_{Total}, is the total ion density of H$^+$, He$^+$, and O$^+$. The density ratio between He$^+$ and H$^+$ ($R_{He/H}$) can be obtained from *Craven et al.* [1997]:

$$\log_{10} R_{He/H} = -1.541 - 0.176r + 8.557 \\ \times 10^{-3} P - 1.458 \times 10^{-5} P^2. \quad (2)$$

where r is the distance from the Earth center in R_E, and P is defined as $P = (F_{10.7} + F_{10.7A})/2$, where $F_{10.7A}$ is the 81-day average of the daily 10.7 cm solar flux ($F_{10.7}$). The observation values of $F_{10.7}$ can be obtained from Space Physics Interactive Data Resource at NOAA (http://spidr.ngdc.noaa.gov/spidr/). Equation 2 is valid only in the plasmasphere for $r \leq 4.5\ R_E$. According to *Lennartsson and Sharp* [1982] and *Denton et al.* [2011], the typical value of $R_{He/H}$ varies from 1% at solar minimum to 3% at solar maximum at geosynchronous orbit. For the two cases considered in this study, $P \approx 190$, so $R_{He/H} = 2.5\%$ at geosynchronous orbit, in consistent with observations. So equation 2 can be used to extrapolate to the outer regions (trough and plume) for the first order approximation in this study.

[13] Assuming that the density ratio between O$^+$ and H$^+$ ($R_{O/H}$) is a constant 1% [*Gallagher et al.*, 2000], then, the He$^+$ density can be obtained by

$$n_{He^+} = \frac{n_{Total}}{1 + R_{He/H} + R_{O/H}} R_{He/H} \quad (3)$$

where n_{Total} is the total ion density.

2.3. Three-Dimensional Density Distributions

[14] Since the DGCPM outputs are SM equatorial plane densities, a 3-D density distribution of the plasmasphere needs to be constructed for intensity integration. The empirical field-aligned density model by *Tu et al.* [2006] is adopted in the density calculation as an ion density model based on the electric neutrality in the plasmasphere. According to *Tu et al.* [2006] model, the electron density $N_e(\lambda)$ along a magnetic field line with L value of L is calculated by the following formulas:

$$N_e(\lambda) = N_0(L) \cos^{-\beta(L)} \left[\frac{\pi \alpha(L) \lambda}{2\ \lambda_{INV}} \right] \quad (4)$$
$$\alpha(L) = A + B \cdot L, \beta(L) = C + D \cdot L$$

where λ and λ_{INV} are the magnetic latitude along a field line and the invariant latitude of the field line, respectively, N_0 is the equatorial plane ion density, namely, the equatorial He$^+$ density obtained in section 2.2. The parameters A, B, C, and D are to be determined by fitting equation 4 to observations. Since no field-aligned N_e distributions from IMAGE radio plasma imager soundings are available for the two storms investigated in this work, the average parameters with $A = 0.99$, $B = 0.005$, $C = 0.5$, and $D = 0.1$ in *Tu et al.* [2006] are adopted. In construction of the 3-D density distribution, the TS07 model is used to calculate the L value of a field line, and λ_{INV} of the field line is defined as the average of the magnetic latitudes of the foot points in the two hemispheres. For points on open field lines, the densities are set to be zero since all plasmaspheric particles are assumed to be trapped on closed field lines [*Lemaire and Gringauz*, 1998].

2.4. Intensity Integration

[15] The He$^+$ density obtained from the DGCPM can be used to calculate the column integrated intensity along a given LOS direction by the equation

$$I = \frac{1}{4\pi} \int_{LOS} e^{-\tau} p(\theta) g n(r) ds \times 10^{-6} \quad (5)$$

where I is the column integrated intensity in rayleigh, and 1 R $= 10^6/4\pi$ photons cm^{-2} s^{-1} sr^{-1}, the phase function reflecting the anisotropy of the scattered radiation is given by $p(\theta) = 1 + 1/4(2/3 - \sin^2\theta)$ [*Brandt and Chamberlain*, 1959], where θ is the angle between the incident direction (Sun-Earth direction) and the scattered direction in the direction of the imager, g is the resonant scattering rate (in photons s^{-1} ion^{-1}) calculated with the method involved in *Garrido et al.* [1994], $n(\mathbf{r})$ is the He$^+$ density in cm^{-3} at position $\mathbf{r}$ obtained in sections 2.2 and 2.3, and τ is the optical depth of 30.4 nm line and can be assumed to be zero since the magnetosphere is optically thin to this emission, and the absorption of magnetospheric species to 30.4 nm emission is extremely small above 1000 km [*Brandt*, 1961; *Meier and Weller*, 1972; *Garrido et al.*, 1994]. The spontaneous emissions and multiple scattering of the helium ions are assumed to be neglected [*Brandt*, 1961; *Meier and Weller*, 1972].

[16] The instrument counts I_C in this study are calculated by the following formula:

$$I_C = I \times S \times T \quad (6)$$

where I is calculated by equation 5; S is the sensitivity of the instrument, $S = 0.12$ count R^{-1} s^{-1} pixel^{-1}; and T is the integration time, $T = 600$ s.
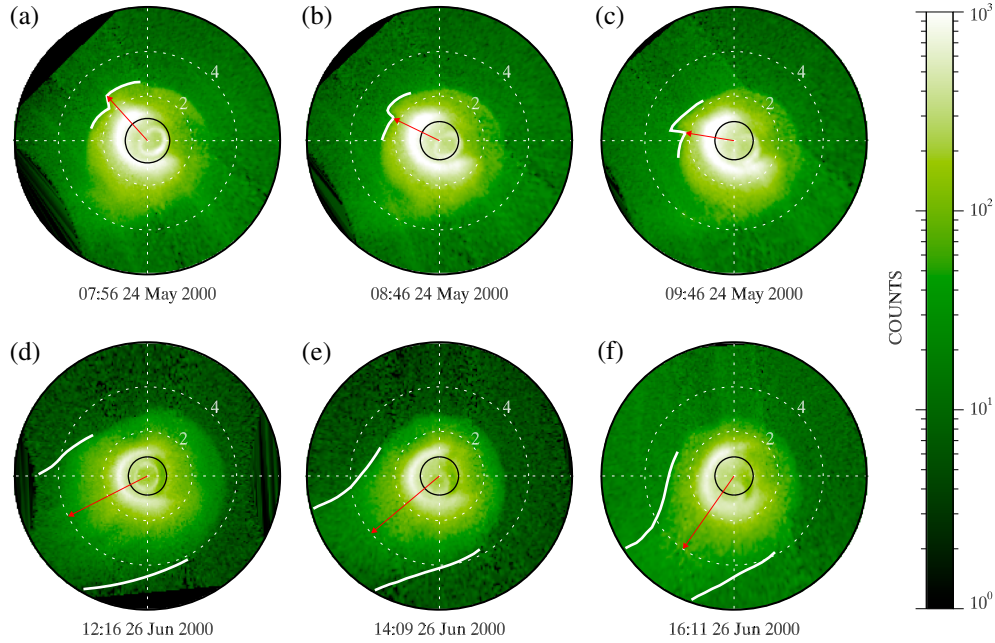
Figure 1. IMAGE EUV images of the plasmasphere at different UTs on (a–c) 24 May 2000 and (d–f) 26 June 2000. The thick white lines represent the manually extracted shoulders in Figures 1a–1c and the unwrapped plumes in Figures 1d–1f in the magnetic equatorial plane in SM coordinate system. The red arrows in Figures 1a–1c represent the longitudinal directions of the shoulders, while the red arrows in Figures 1d–1f represent the longitudinal directions of the plumes. The black circles represent the Earth. The horizontal dashed lines are along the noon-midnight line with noon to the left, while the vertical dashed lines are along the dawn-dusk line with dawn to the up. The dashed circles are drawn at $L = 2, 4$. The log-scaled color bar representing the instrumental counts is shown at the right.

3. Imaging the Plasmasphere From the Moon

[17] In order to investigate the large-scale structures (e.g., plasmapause, plume, and shoulder), emission intensities, and dynamic evolutions of the plasmasphere from lunar perspectives, the storms observed by IMAGE EUV on 24 May 2000 (strong) and on 26 June 2000 (median) are simulated by the DGCPM in this section. It is expected that the simulations of these two storms will provide us basic pictures of the plasmasphere during active and moderate SW-IMF conditions in the moon-based EUV imaging.

[18] To emphasize the differences between polar imaging and moon-based imaging, only IMAGE EUV observations are presented in Figure 1 (all projected in SM equator), and the detailed studies and simulations of the two storms from polar orbit can be found in *Goldstein et al.* [2002] and *He et al.* [2010b]. Figures 1a–1c are for the storm on 24 May 2000 and Figures 1d–1f are for the storm on 26 June 2000. The plume and shoulder of the plasmasphere in Figure 1 are manually extracted in the images where the emission intensity drops abruptly at the boundary using the method described in literatures [e.g., *Roelof and Skinner*, 2000; *Sandel et al.*, 2003]. It is shown that the configurations of the plasmasphere change little with observation positions but dramatically with SW-IMF conditions, and the latitudinal distribution information of the plasmaspheric structures (plasmapause, shoulders, plumes, etc.) cannot be obtained from the polar-orbiting images.

[19] A virtual EUV imager is placed on the moon and views toward the center of Earth with an FOV of 15°, corresponding to a spatial size of 15.0 R_E on the projection plane that contains the center of Earth and is perpendicular to the axis of the FOV of the imager, assuming the average Earth-to-Moon distance to be 60.0 R_E. The spatial resolution of the image on the projection plane is 0.1 R_E with an equivalent angular resolution of 0.095°. The sensitivity, integration time, and sensitivity threshold of the imager are 0.12 count R^{-1} s^{-1} pixel^{-1}, 10 min, and 0.1 count min^{-1} pixel^{-1}, respectively, for all the simulations below. Twelve points in the lunar orbit in Figure 2 are selected to investigate the radiation intensity distributions from different lunar phases, and the coordinates of these points are all in SM in R_E. Three points are selected during adjacent lunar phases. The points located in the first quarter moon to the full moon sector of the lunar orbit are marked with d (−51.4, 21.9, 11.9), e (−39.9, 40.8, 9.0), and f (−22.0, 54.3, 4.8), and the points located in the full moon to the last quarter moon sector of the lunar orbit are marked with a (−21.8, −54.3, 5.5), b (−39.7, −40.8, 9.5), and c (−51.3, −21.9, 12.2). The remaining six points are symmetric to above points with respect to the Y_{SM} axis. When transformed to GSE coordinate system, the 12 points are symmetrically located around the new moon-to-full moon line. It is necessary to point out that the Earth's tilt angle is not considered in *He et al.* [2010b], resulting that the moon-based images are almost north-to-south symmetric. The effects of the Earth's tilt angle on the simulated images will be considered in this investigation.
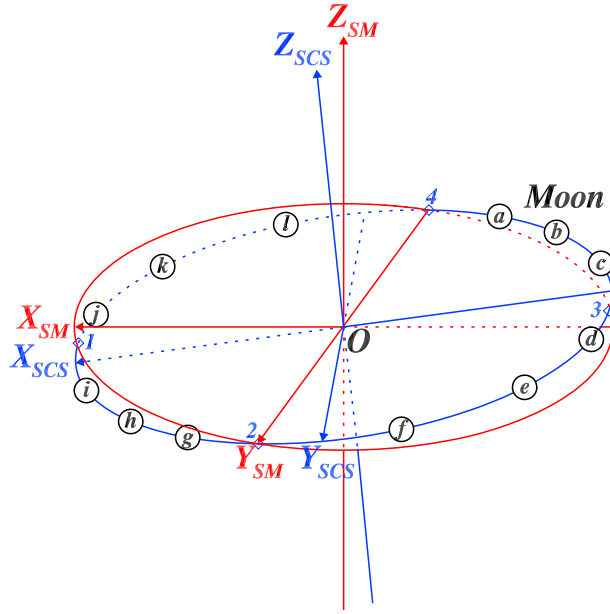
Figure 2. Illustration of the SCS and the SM coordinate systems. The 12 black circles represent the positions of the moon used in section 3. The four diamonds represent the lunar phases with the first for the new moon, the second for the first quarter moon, the third for the full moon, and the fourth for the last quarter moon. The X_{SCS} axis is along the axis of the FOV of the imager, while the other axes are determined by rotating of corresponding SM axes and obey the right-hand law.

3.1. Imaging From Different Views

[20] The EUV images simulated at different positions of the lunar orbit at 08:46 UT on 24 May 2000 and at 14:09 UT on 26 June 2000 are shown in Figures 3 and 4, respectively. All images are projected in the yz plane in the satellite coordinate system (SCS) as defined in Figure 2. In the following sections, the horizontal direction is from left to right along the SCS y axis, and the vertical direction is from down to up along the SCS z axis.

3.1.1. He$^+$ Emission Intensity

[21] When the simulated instrument counts are converted to rayleigh according to equation 6, the intensities from the main body of the plasmasphere within the sharp edges are $0.1 \sim 11.91$ R in Figure 3 and $0.1 \sim 12.27$ R in Figure 4, which are in consistent with the early sounding rocket measurements of $0.1 \sim 10$ R [*Ogawa and Tohmatsu*, 1971; *Paresce et al.*, 1973], the simulated intensity of $0.1 \sim 15.0$ R [*Roelof et al.*, 1992], and the Planet-B mission measurements of $0.1 \sim 7.0$ R [*Nakamura et al.*, 2000]. The intensity in the plasmaspheric trough outside the plasmapause is approximately $0.02 \sim 0.1$ R. The He$^+$ density beyond the plasmapause is quasi-stable during quiet periods and has a density of 0.2–$2.0\,\mathrm{cm}^{-3}$ inferred from the DGCPM simulations and the Geotail measurements [*Matsui et al.*, 1999], and the corresponding column integrated intensity is 0.026–0.13 R. However, it is found that the He$^+$ density outside the plasmapause can increase to 4–20 cm^{-3} during disturbed periods (e.g., main phase of the storm) [*Yoshikawa et al.*, 2001], and the column integrated intensity is expected to achieve approximately 0.1 R in plasmaspheric trough. The maximum intensity in Figure 4 is larger than that in Figure 3

because the contribution of the plume ions to the integration in Figure 4 is larger.

3.1.2. Perspective Effects

[22] It is noted that there exists a north-to-south asymmetry in the simulated images in Figures 3 and 4. This asymmetry in the SCS is resulted from the facts that the imager is not located on the SM equatorial plane, and the tilt angles between the SM equatorial plane and the plane of the lunar orbit are approximately +18.3° for 24 May 2000 storm and +16.4° for 26 June 2000 storm, respectively, even when the plasmasphere is north-to-south symmetric in SM.

[23] The simulations demonstrate that the plasmaspheric shoulders might have two types of configurations in the moon-based images: the meniscus-shape shoulders indicated by the dashed meniscus regions in Figures 3a–3c and 3g–3i and the step-shape shoulders indicated by the dashed rectangle regions in Figures 3d, 3e, 3j, and 3k. The shoulders are not notable at other positions because of the shading of the main body of the plasmasphere. It is found that the spatial sizes of the shoulder are ~0.4 R_E in horizontal direction in Figures 3a–3c and 3g–3i and are ~0.3 R_E and ~0.4 R_E in vertical direction in Figures 3d, 3e, 3j, and 3k, respectively. These differences in size are caused by the different projection patterns and shading of the main body of the plasmasphere.

[24] The shape and position of the plumes marked with the white arrows in Figures 3 and 4 change dramatically with the modeling positions since the LOS directions and the projection directions are different. The wrapped plume appears to surround the main body of the plasmasphere from side view in Figure 3. When the longitudinal direction of the plume (~15:00 magnetic local time (MLT) on equatorial plane as indicated by the red arrow in Figure 1e) is orthogonal to the axis of the FOV of the imager, the plume in the image is attached to the plasmasphere and shows a diffusive distribution as shown in Figures 4a, 4d–4g, and 4j–4l. Nevertheless, when viewed from the longitudinal direction of the plume, it will be vertically located in the center of the images in Figures 4b, 4c, 4h, and 4i. With the plumes lengthening and narrowing on the equatorial plane, the plumes in the images extend vertically. Since the plasmapause is irregular on equatorial plane, imaging from different positions, the main bodies of the plasmasphere in the moon-based images as shown in Figures 3 and 4 are also different.

3.1.3. Earth's Shadow Effects

[25] The Earth's shadow effect is generated by the shading of the EUV emissions by the Earth. The Earth's shadows mainly contain two parts in imaging the plasmasphere, one is caused by the shadow behind the Earth in the view of the Sun and the other is the shadow in the FOV of the imager as shown in Figure 5. Both are clearly noted in Figures 3 and 4 in which the shadows are significantly different from those in Figure 1.

[26] For an imager orbiting in the Earth's polar orbit (e.g., IMAGE), the two parts of Earth's shadows are shown by the red cylinder "A" and the blue cones "F$_1$", "F$_2$", and "F$_3$" in Figure 5a. "A" is unchanging with the satellite positions, while "F$_1$", "F$_2$", and "F$_3$" change with the satellite positions. Take IMAGE orbit for an example. The imaging is carried out in the apogean region of the polar orbit, and the images are projected on SM equatorial plane, so "F$_1$", "F$_2$", and "F$_3$" correspond to polar region of plasmasphere, where the densities in the blue cone regions are very low, and their contributions to the intensity integration are also small. Thus, the Earth's shadows in the IMAGE EUV images in Figure 1
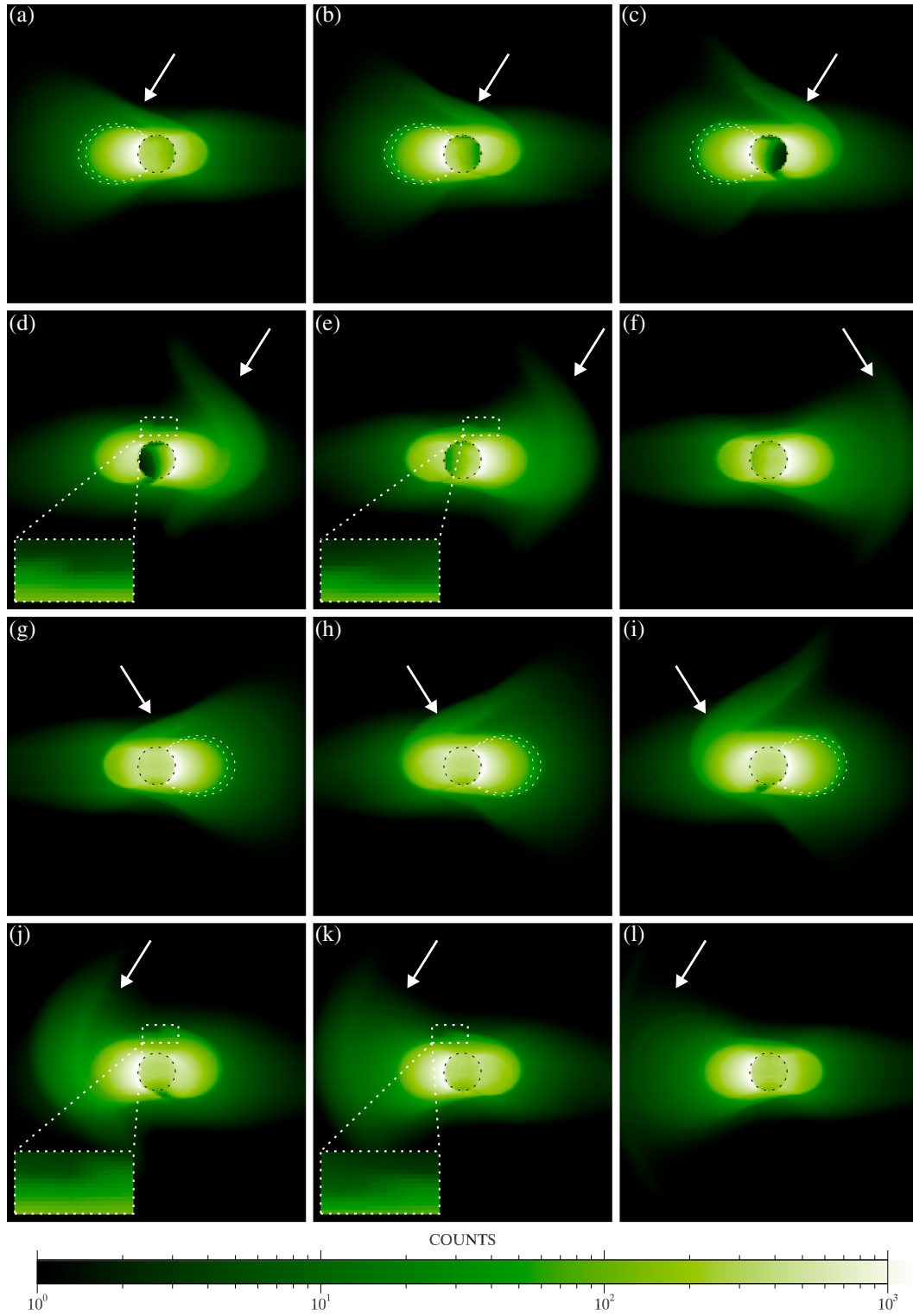
Figure 3. Modeled EUV images for the 12 positions in Figure 2 at 08:46 UT on 24 May 2000. The dashed black circles represent the Earth. The dashed rectangles and meniscus represent the region of shoulders. (a–c and g–i) The L values of the dipole field lines are 3.8 and 4.3. The plumes are indicated by white arrows. (d–e and j–k) The dashed rectangles at the lower left corners represent the magnified views of shoulder regions, and the log-scaled color bar is shown at the bottom.
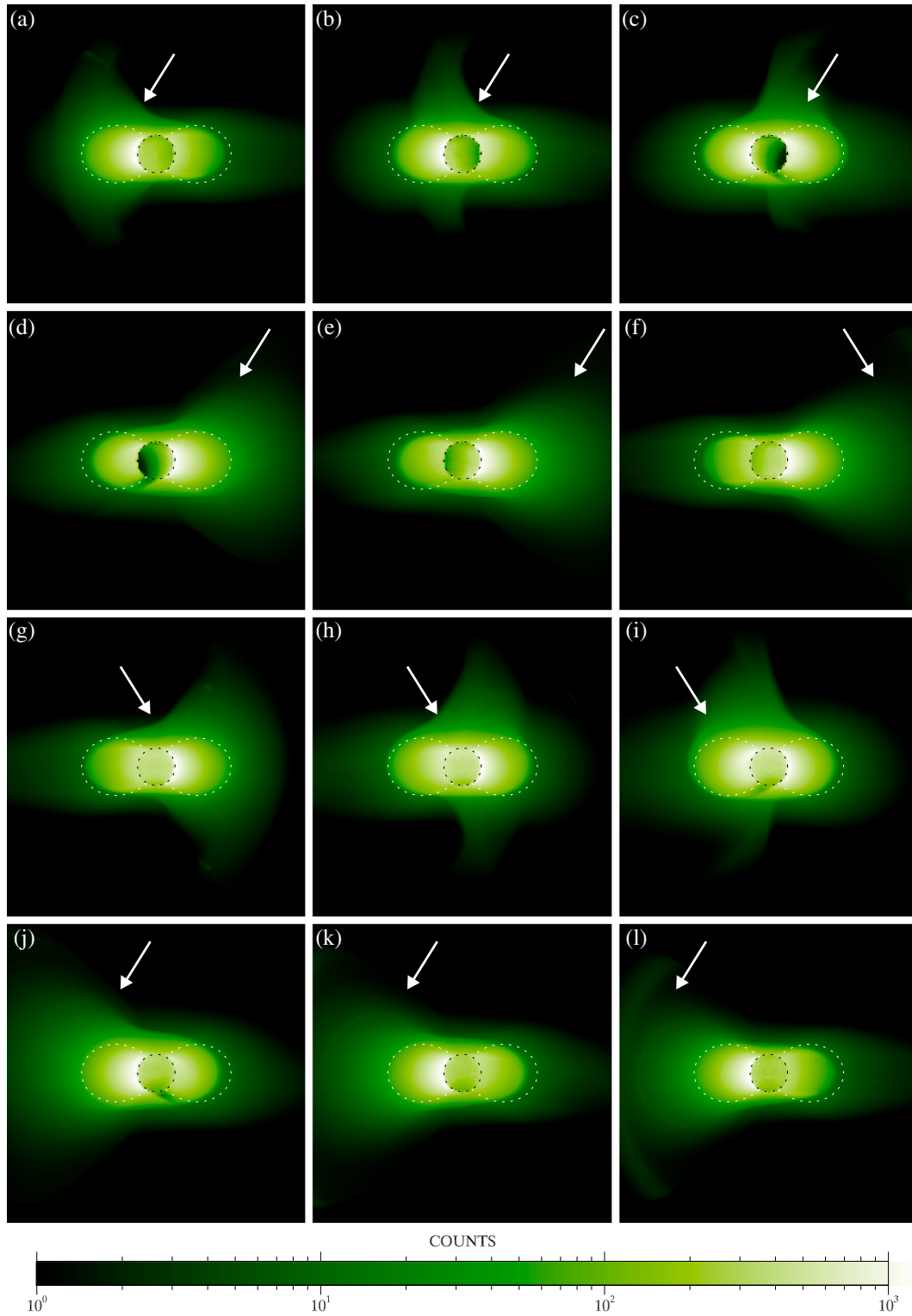
Figure 4. Modeled EUV images for the 12 positions in Figure 2 at 14:09 UT on 26 June 2000. The plumes are signed by the white arrows. The log-scaled color bar is shown at the bottom. The dipole field line with L value of 4.0 is shown by dashed white line.

change little with the satellite positions around the apogee. The shadows in the projected images in Figure 1 almost always lie in the horizontal direction at nightside.

[27] For moon-based imaging, the shadow "A" is also unchanging but its projection on the images changes with the

lunar positions. The shadow "F_M" changes dramatically with the lunar positions. Since the lunar orbit is tilted to the SM equatorial plane, when the imager is near the first quarter moon or the last quarter moon, e.g., position f or a in Figure 2, the moon is almost in the SM equatorial plane; thus,
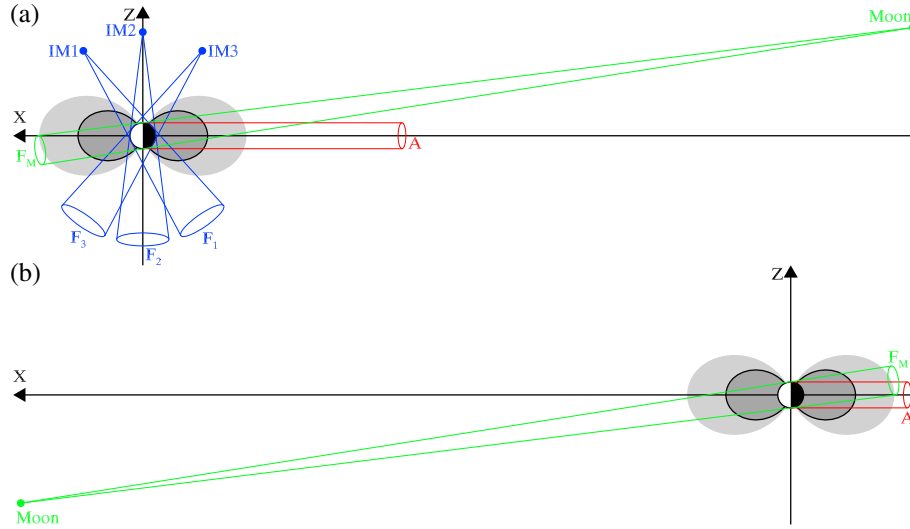
Figure 5. Illustration of the Earth's shadows for the polar orbiting imager (IMAGE) and the moon-based imager in the SM *xz* plane for (a) the full moon (b) the new moon. The red cylinder represents the shadow behind the Earth in the view of the Sun. "IM1", "IM2", and "IM3" represent three typical positions of IMAGE mission in different seasons. The blue cones marked by "F_1", "F_2", and "F_3" represent the shadows in the FOV of IMAGE corresponding to the three IMAGE positions. The green cones marked by "F_M" represent the shadow in the FOV of the moon-based imager. The thick black dipole field line represents the plasmapause; the deep gray region inside is the main plasmasphere while the gray region outside is the plasmaspheric trough. All cones are just the parts of FOV shaded by the Earth, not the true FOV of the imagers.

the projections of the shadow "A" in the simulated images (see Figures 3a, 3f, 4a, and 4f) are nearly along the horizontal directions since the projection plane is almost parallel to the SM *xz* plane and have little overlap with the projections of shadow "F_M" which are in the center of the images. In such cases, the effects of these two types of shadows are independent, and the shadows in the images are not significant.

[28]   When the imager is near the full moon, e.g., position *c* or *d* in Figure 2, the projection of the shadow "A" is tilted to the lower right corner in Figures 3c and 4c and to the lower left corner in Figures 3d and 4d with the tilt angle proportional to the latitude of the imager in SM. The shadows "A" and "F_M" in Figure 5a are located at nightside and dayside, respectively, and the amount of the shaded plasmaspheric ions is the largest. It is noted in such cases that the shadow "A" overlaps the shadow "F_M" and the shadows in the images are significant, like a comma "," shape. When the imager is near the new moon, e.g., position *i* or *j* in Figure 2, however, both the shadows "A" and "F_M" in Figure 5b are located at nightside, and the amount of the shaded plasmaspheric ions is greatly less than that of the full moon. Hence, the shadows in Figures 3i and 3j or 4i and 4j are not as notable as those in Figures 3c and 3d or 4c and 4d.

3.2.   Time Evolution of Plasmaspheric EUV Images From the Moon

[29]   Based on understanding of the plasmaspheric properties from lunar perspectives in section 3.1, the time evolution of the plasmaspheric EUV images from the moon is discussed in this section so as to further assess the temporal evolution property of the moon-based EUV imaging.

3.2.1.   Storm on 24 May 2000

[30]   The temporal evolutions of the plasmasphere for storm on 24 May 2000 are shown in Figure 6 for positions

a, *b*, *c*, and *d*; in Figure 7 for positions *e*, *f*, *g*, and *h*; and in Figure 8 for positions *i*, *j*, *k*, and *l*. The evolutions imaged from the moon exhibit absolutely different patterns compared with IMAGE EUV imaging.

[31]   At 07:56 UT, the shoulder is at the dawn sector with a small radial size, and its outer boundary is smooth on the equatorial plane as shown in Figure 1a. Thus, the shoulder is not significant in Figures 6–8 (first column). As time goes on, the shoulder rotates toward noon and becomes wider in radius as seen from polar orbit, and its average rotating speed is ~1.13 h of MLT per hour at the outer edge in Figure 1. Correspondingly, the shoulder behaves as moving toward the center of the images and becomes vertically wider if viewed from positions *d*, *e*, *j*, and *k* (see Figures 6d, 7e, 8j, and 8k) or behaves as diffusing to outer space surrounding the plasmapause if viewed from the full moon to the last quarter moon sector or from the new moon to the first quarter moon sector of the lunar orbit, especially at position *a* (see Figure 6a). It is demonstrated that the meniscus-shape shoulder can only be observed from the full moon to the last quarter moon sector or from the new moon to the first quarter moon sector of the lunar orbit, while the step-shape shoulder can only be observed from the first quarter moon to the full moon sector or from the last quarter moon to the new moon sector.

[32]   According to the LOS projection patterns of the moon-based imaging and the magnetic field model (TS07) used in the simulation, when traced back onto the SM equatorial plane, the longitudinal positions of the step-shape shoulders indicated by the dashed rectangles are 09:02, 10:10, and 11:15 MLT in Figures 6d, 7e, 8j, and 8k, respectively, which are in consistent with that deduced from polar orbit images in Figures 1a–1c. The radial position of the inner edge of the shoulders is ~3.8 R_E which
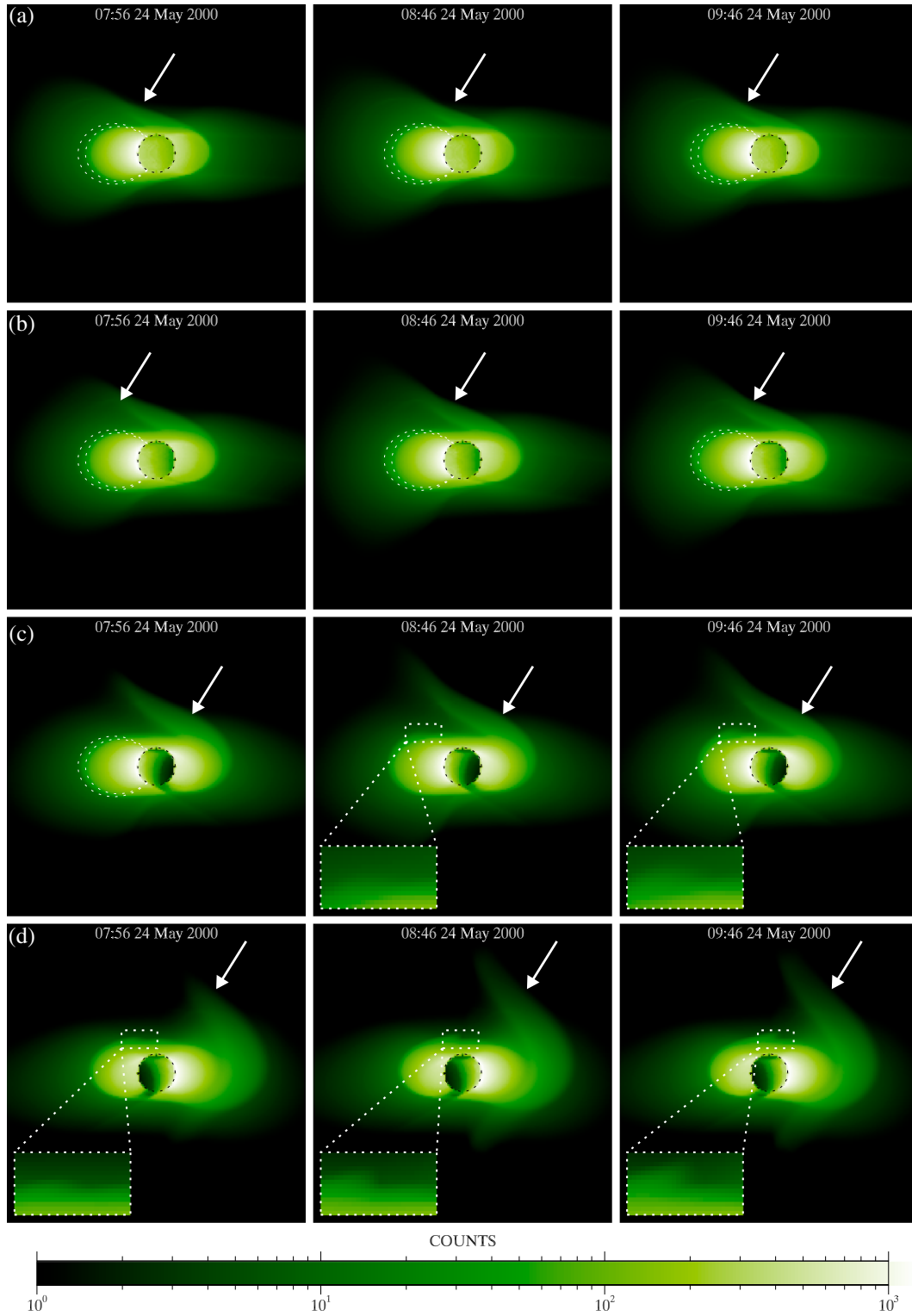
Figure 6. EUV images of the plasmasphere for the 24 May 2000 storm for positions *a*, *b*, *c*, and *d*. The dipole field lines with *L* values of 3.8 and 4.3 in rows 1–3 are the average positions of the inner edge and outer edge of the shoulder at 07:56 UT. Other format is the same as that of Figure 3.

is slightly larger than IMAGE observations of ~3.0 R_E. This is probably because the magnetic field pattern embedded in the simulation is different from the actual pattern, and the dayside convection electric field is stronger than the actual electric field, resulting that the sunward convection becomes stronger. The vertical widths of the shoulders are 0.2 R_E, 0.3 R_E, and 0.4 R_E in Figure 6d and are 0.2 R_E, 0.4 R_E, and 0.5 R_E in Figure 8j, respectively. It is noted that the differences are caused by projection patterns. The corresponding radial widths on SM equatorial
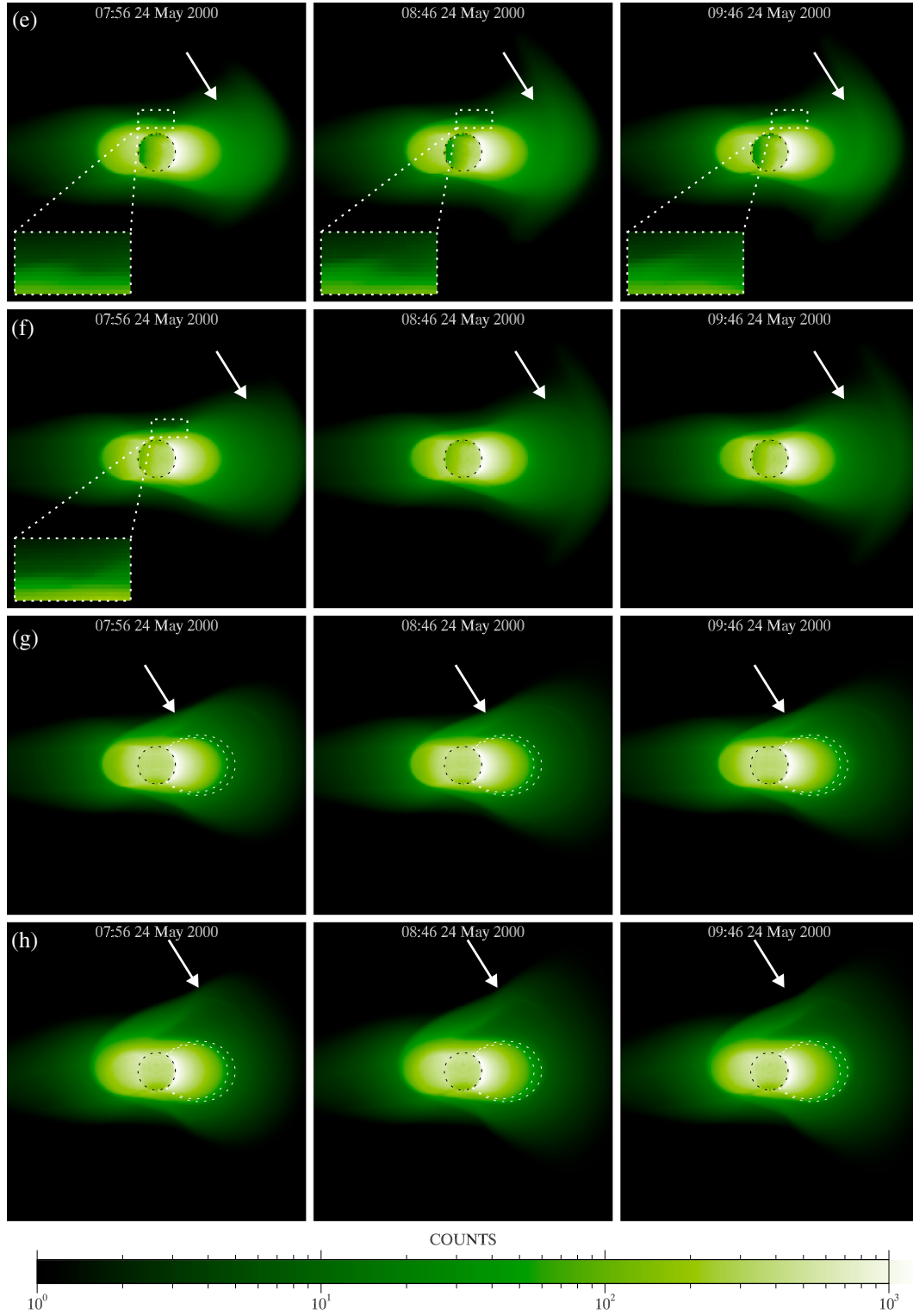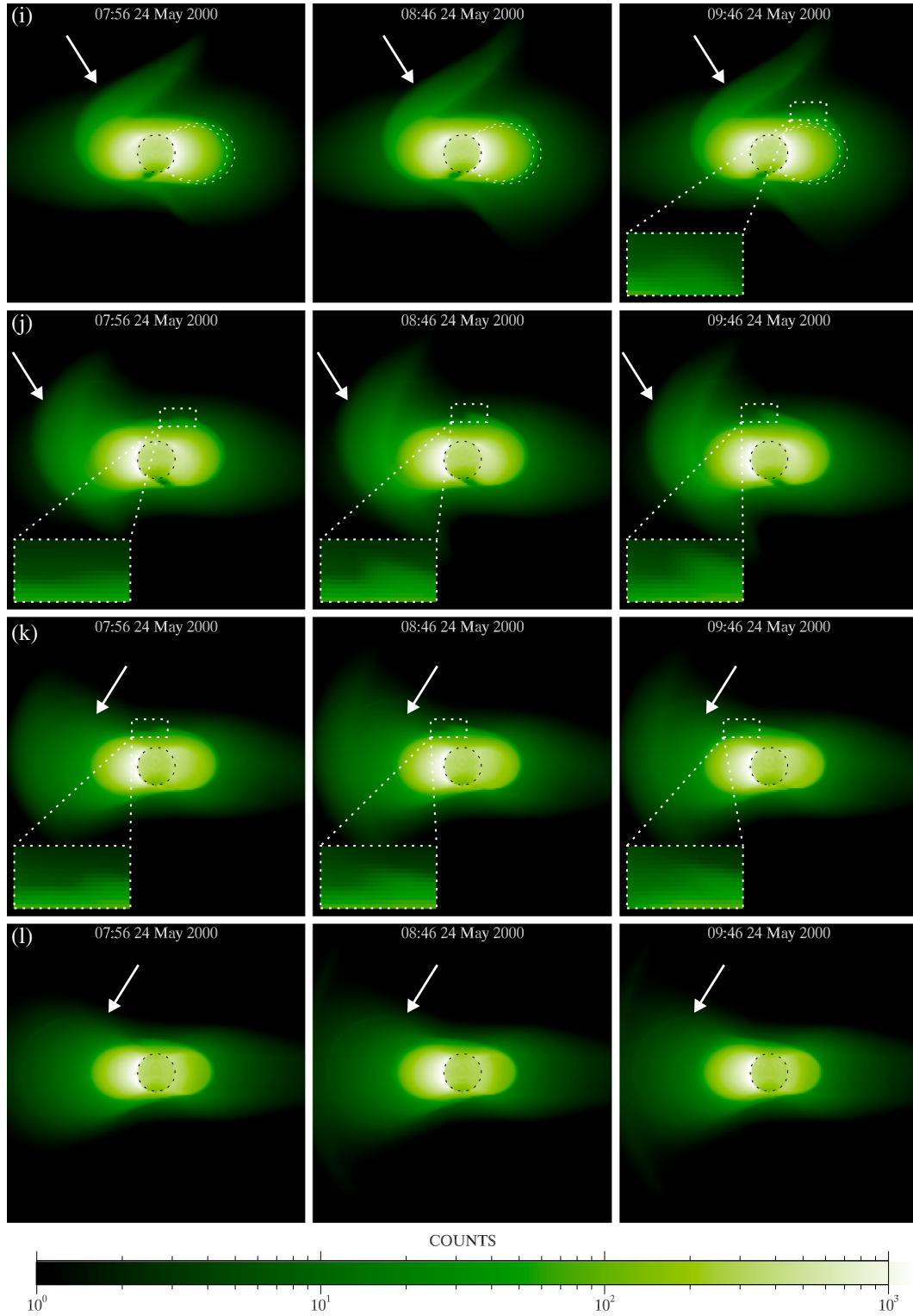
Figure 7. EUV images of the plasmasphere for the 24 May 2000 storm for positions *e*, *f*, *g*, and *h*. Other format is the same as that of Figure 6.

plane are 0.5 R_E, 0.6 R_E, and 0.8 R_E, respectively, which are also in consistent with polar orbit images in Figures 1a–1c. The fact that the outer edge of the shoulder rotates faster than the inner edge on the equatorial plane, as discussed both in our simulation and early research [*Goldstein et al.*, 2002], is exhibited as edge sharpening

in vertical direction modeled from the moon, i.e., the upper part of the shoulder moves faster than the lower part (see Figures 6d and 8j).

[33] When the imager is located at position *b* or *h*, the shoulder is not shaded by the main body of the plasmasphere in the LOS integrations at these three UTs (see Figures 6b or
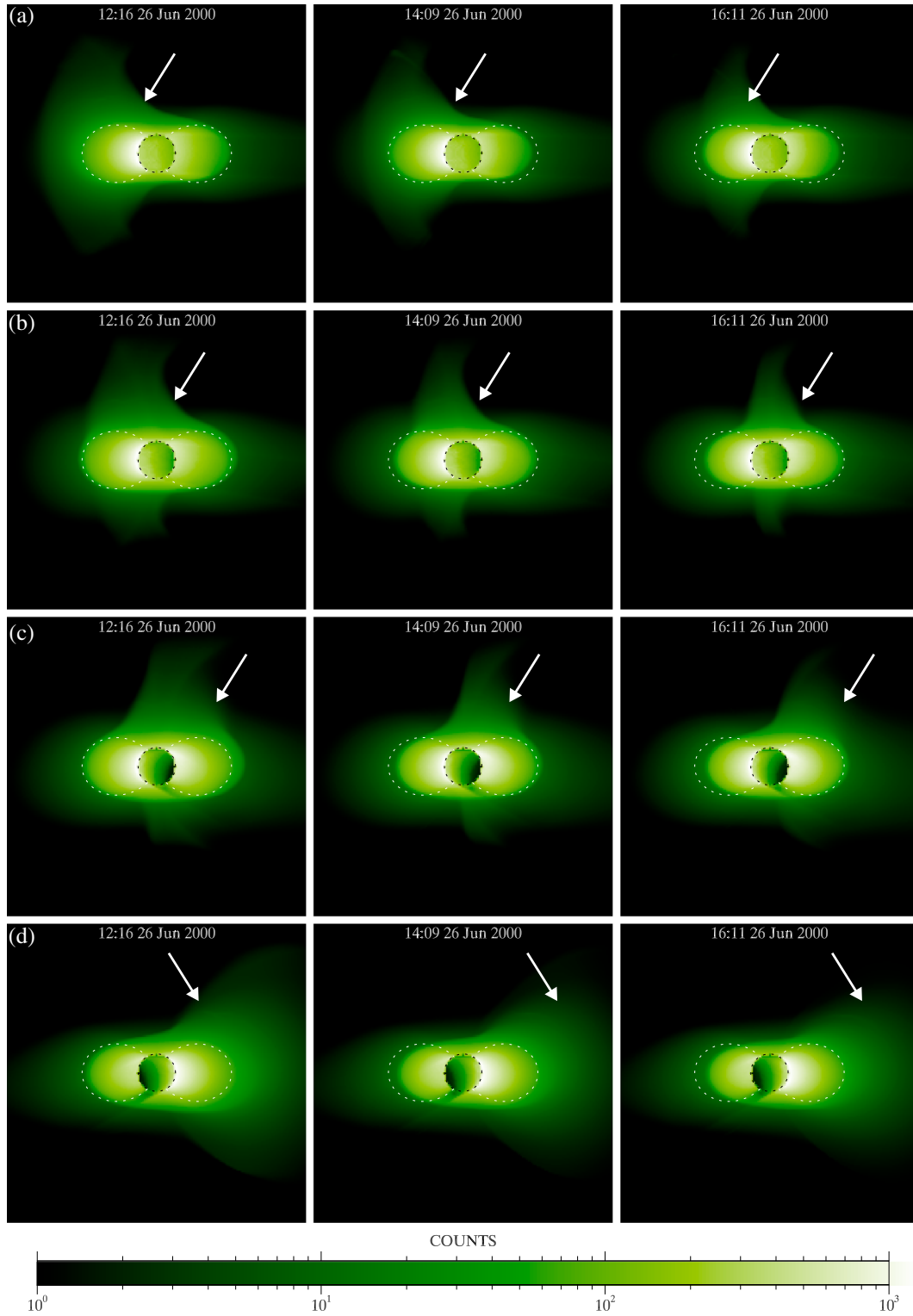
Figure 8. EUV images of the plasmasphere for the 24 May 2000 storm for positions *i*, *j*, *k*, and *l*. Other format is the same as that of Figure 6.

7h), and the moon-based images clearly reveal the latitudinal configuration of the shoulder. For the case of position *a*, the shoulder is shaded at 07:56 UT, and it is not clear in the first panel of Figure 6a. The meniscus-shape shoulders do not move in the images but change their widths in horizontal direction because the shoulders rotate and change their radial widths in the equatorial plane and the shading of the plasmasphere is different.

[34] It can be concluded from the simulations that the latitudinal distribution of the shoulder can only be observed at direction perpendicular to the longitudinal direction of the shoulder as shown by the red arrows in Figures 1a–1c,
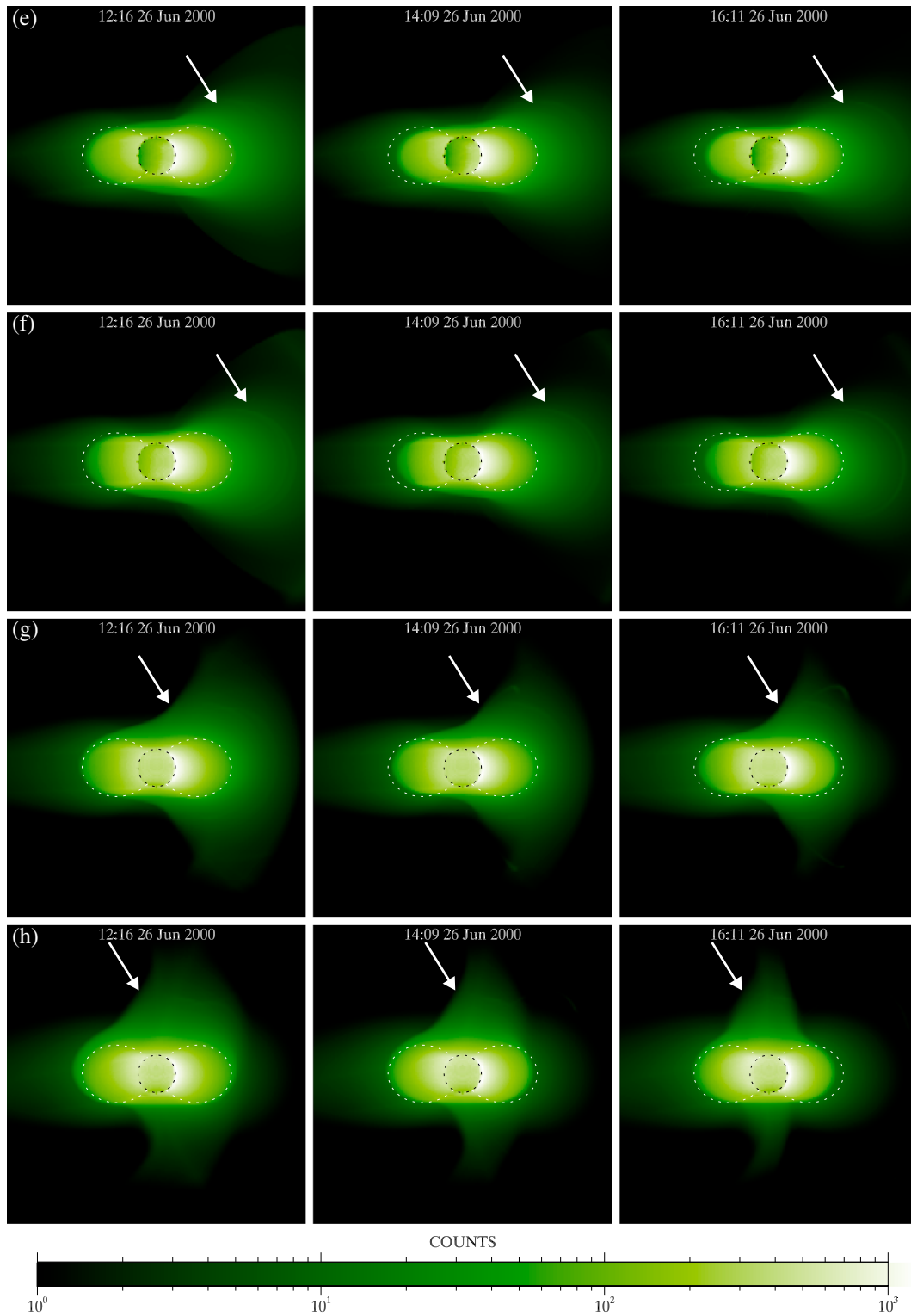
Figure 9. EUV images of the plasmasphere for the 26 June 2000 storm for positions *a*, *b*, *c*, and *d*. The dipole field line with *L* value of 4.0 is shown by dashed white lines. Other format is the same as that of Figure 4.

whereas the motion of the0 shoulder can only be observed at direction parallel to the longitudinal direction of the shoulder.

3.2.2. Storm on 26 June 2000

[35] The temporal evolutions of storm on 26 June 2000 are shown in Figure 9 for positions *a*, *b*, *c*, and *d*; in Figure 10 for positions *e*, *f*, *g*, and *h*; and in Figure 11 for positions *i*, *j*, *k*, and *l*. The main body of the plasmasphere in Figures 9–11 has little difference from that of Figures 6–8. However, large differences exist in the outer parts of the plasmasphere.
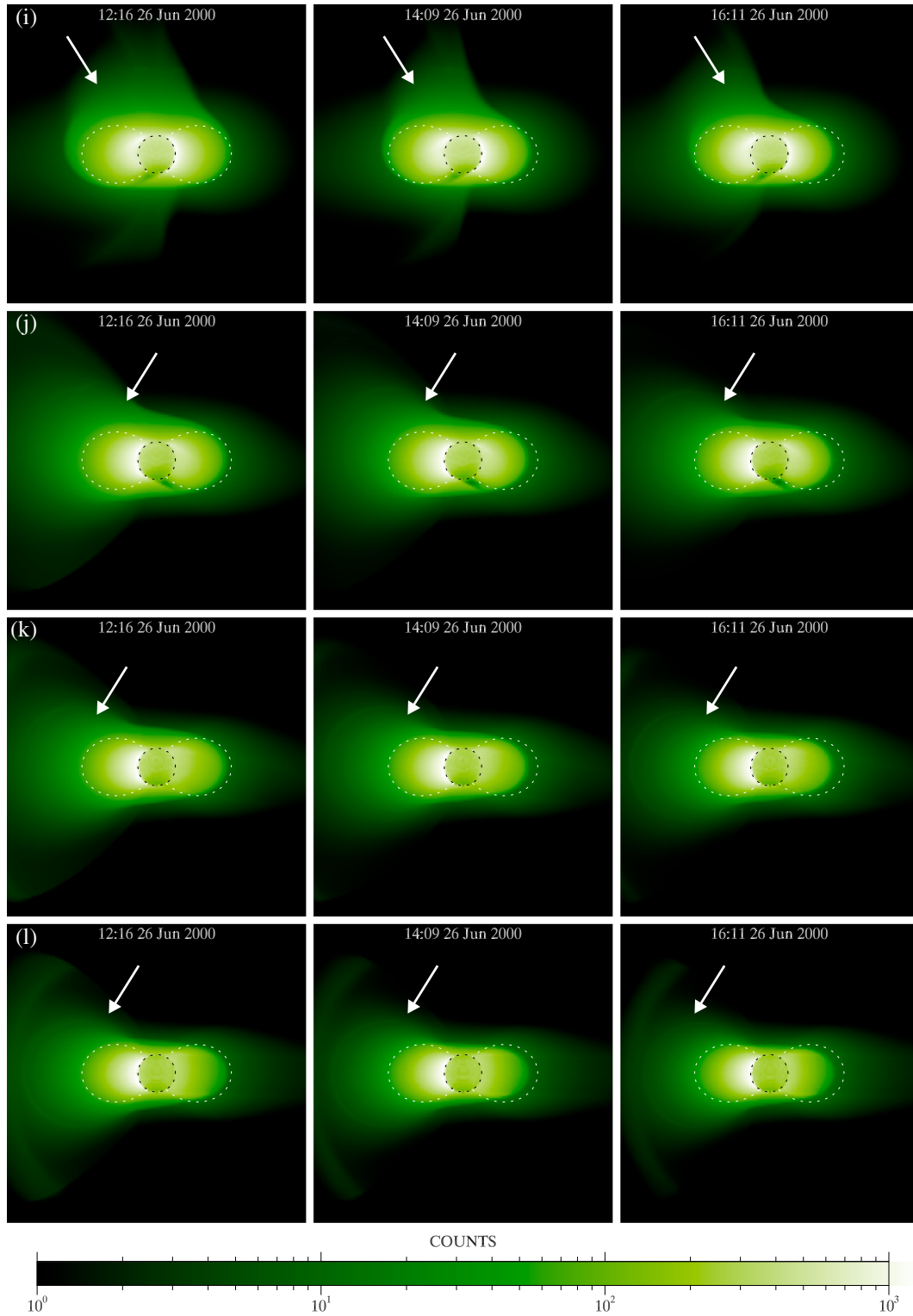
Figure 10. EUV images of the plasmasphere for the 26 June 2000 storm for positions *e*, *f*, *g*, and *h*. Other format is the same as that of Figure 9.

[36] In the case of 26 June 2000 storm, the plasmaspheric plume rotates duskward and becomes longitudinally narrow, and the outer parts of the images (region of plumes) of Figures 9–11 are shrunken and darkened. The plume is directly connected to the main body of plasmasphere in Figures 1d–1f without wrapping, and thus, the gap between the plume and the plasmapause is not significant or no gap exists. In the case of 24 May 2000 storm, however, the plumes are wrapped in Figures 1a–1c, so the gap between the plume and the plasmapause in Figures 6–8 is significant.

[37] When the imager is located at the first quarter moon to the full moon sector or at the last quarter moon to the new

Figure 11. EUV images of the plasmasphere for the 26 June 2000 storm for positions *i*, *j*, *k*, and *l*. Other format is the same as that of Figure 9.

moon sector of the lunar orbit, the imaging directions are approximately perpendicular to the longitudinal directions of the plumes, which appear diffusive distributions outside the plasmapause, and the latitudinal distribution of the plumes can be seen in Figures 9d, 10e, 10f, and 11j–11l. However, when the imager is located at the full moon to the last quarter

moon sector or at the new moon to the first quarter moon sector, especially at position *b* or *h*, the longitudinal direction of the plume on the SM equatorial plane is nearly parallel to the imager-to-Earth line, and thus, the plumes in the images in Figures 9b, 9c, 10h, and 11i are all along the vertical directions. From 12:16 UT to 16:11 UT, the plumes in the images

move from left to right and become narrow in horizontal direction. When the plume silhouettes in the three images are traced back onto the SM equatorial plane, it is shown that the plumes rotate toward dusk and become narrowing, which is in consistent with observations. Erosion of the main body of the plasmasphere is also clear as shown by the dashed dipole field lines in Figures 9–11.

4. Discussion

[38] The EUV imager on the CE-3 mission will continuously image the overall plasmasphere from the moon. The continuous imaging period is approximately 27 days during one lunar period (there is ~1.4 days around the full moon when the angle between the sunlight and the axis of the FOV of the imager is less than half of the FOV, and the sunlight can enter the imager which must be shut down). However, due to the power limitation of the lunar lander (hope this limitation can be solved in the next mission), the moon-based EUV imager will only image the plasmasphere during the first quarter moon to the last quarter moon, and the continuous observation period is ~12 days during one lunar period.

[39] It is expected that this might provide us with the longest and continuous imaging period compared with all previous imagers [*Nakamura et al.*, 1999; *Sandel et al.*, 2000; *Sasaki et al.*, 2003] so as to advance the understanding of the plasmasphere-related questions that have not been solved by past observations. Discussions below will demonstrate that the moon-based EUV imaging might provide us with new characteristics of the global structures and dynamic evolutions of the plasmasphere and also indicate that this simulation may give us the comprehensive understanding on moon-based EUV images and the relationship between the moon-based EUV images and the plasmaspheric dynamics.

4.1. Intensity Distribution and Global Images of the Plasmasphere

[40] In this simulation, the emission intensity is assumed to be only contributed by the He^+ 30.4 nm emission from the plasmasphere without considering the contaminations from other wavelengths or other origins, in order that we can clearly catch the global distributions of the plasmaspheric emission intensity in the images and easily discover new structures and new evolution patterns in the moon-based EUV images.

[41] For the design of the CE-3 EUV imager and the further EUV image inversion, three noise sources should be considered. The first part is the instrumental background noise from the microchannel plates in the detector, which is too low to affect the signal-to-noise ratio (SNR) compared with the signal counts. The second part is the contamination from the He I 58.4 nm and the H Ly α emissions. The metallic filter is almost opaque to the Ly α emission which has little effect on SNR. It is known that the geocoronal 58.4 nm emission is mainly under the height of 2000 km with a maximum intensity of ~500 R [*Meier*, 1991], and the interplanetary 58.4 nm emission is almost uniform throughout the FOV of the imager with intensity of ~1.5 R [*Wu et al.*, 1981; *Jelinsky et al.*, 1995]. According to the spectra responses of the filter, the multilayer mirror, and the detector of CE-3 EUV at 30.4 nm and 58.4 nm, the sensitivity ratio of

30.4 nm to 58.4 nm is ~79.0 for CE-3 EUV, and the overall SNR in the whole FOV is greater than 2.0, and the SNRs in the main plasmasphere, plasmapause, and plume regions are greater than 3.0 in the common mode of CE-3 EUV (10 min exposure and 0.095° angular resolution). Therefore, the global structures of the plasmasphere can be grasped and identified with CE-3 EUV.

[42] The third part is the 30.4 nm emissions from other sources, such as interplanetary space and He^+ born by charge-exchange collisions [*Gruntman*, 2001] between the solar wind alpha particles (He^{2+}) and the local atomic hydrogen (H) in the magnetosheath. It is known from the literatures that the interplanetary 30.4 nm emission is approximately uniform and extremely low with intensity to be ~0.001 R [*Paresce et al.*, 1981; *Jelinsky et al.*, 1995; *Gruntman*, 1992, 2001; *Gruntman et al.*, 2006]. For the case of solar wind charge exchange (SWCX), the intensity is related to the densities of solar wind He^{2+} and local H, the solar wind velocity, and the He^{2+}-H charge exchange cross section ($\sigma_{30.4}$) which is strongly dependent on collision velocity [*Gruntman*, 2001; *Gruntman et al.*, 2006]. Take the subsolar magnetopause for an example. The large density of H at subsolar magnetopause is ~100 cm^{-3} [*Paschmann et al.*, 1978], the typical He^{2+}/H ratio in the magnetosheath is 5%, and $\sigma_{30.4} = 6.275 \times 10^{-16} cm^2$ at a high solar wind speed of 750 $km s^{-1}$ [*Gruntman et al.*, 2006]. Assuming the LOS integration length to be 4.0 R_E (the distance between the magnetopause and the bow shock along the Sun-Earth line) and these parameters are constants along the LOS, the emission intensity is estimated to be ~0.005 R (equivalent to ~0.4 instrumental counts) given by *Gruntman et al.* [2006, formula 1]. Therefore, the emission intensity from the SWCX is below the sensitivity threshold of CE-3 EUV and might have little influence on the moon-based EUV imaging. Detailed discussion and simulation of the 30.4 nm emission intensity from the SWCX in the moon-based imaging will be discussed in the future.

4.2. New Characteristics of Moon-Based EUV Imaging

[43] Modeled EUV images display new characteristics which can help us study the real time images of the moon-based EUV imager and catch the global structures of the plasmasphere. The new characteristics are as follows:

[44] 1. The main body of the plasmasphere exhibits new shape in the moon-based EUV images. Observed by IMAGE EUV, the main body of the plasmasphere is approximately circular [*Sandel et al.*, 2003], whereas in the moon-based images, the main body of the plasmasphere is elliptical and more or less coincides with the shapes of field lines.

[45] 2. Different from IMAGE observations, the shoulder of the plasmasphere has two types of shapes with different evolution patterns in the moon-based images. The shoulders may have step-like shapes in the upper parts of the images and move to the center with time when the imager is located in the first quarter moon to the full moon sector or the last quarter moon to the new moon sector of the lunar orbit (see Figures 6d, 7e, 8j, and 8k) or may appear meniscus-like shapes surrounding the plasmapause in the left or right side of the images when the imager is located at the full moon to last quarter moon sector or the new moon to the first quarter moon sector (see Figures 6a, 6b, 7g, and 7h).
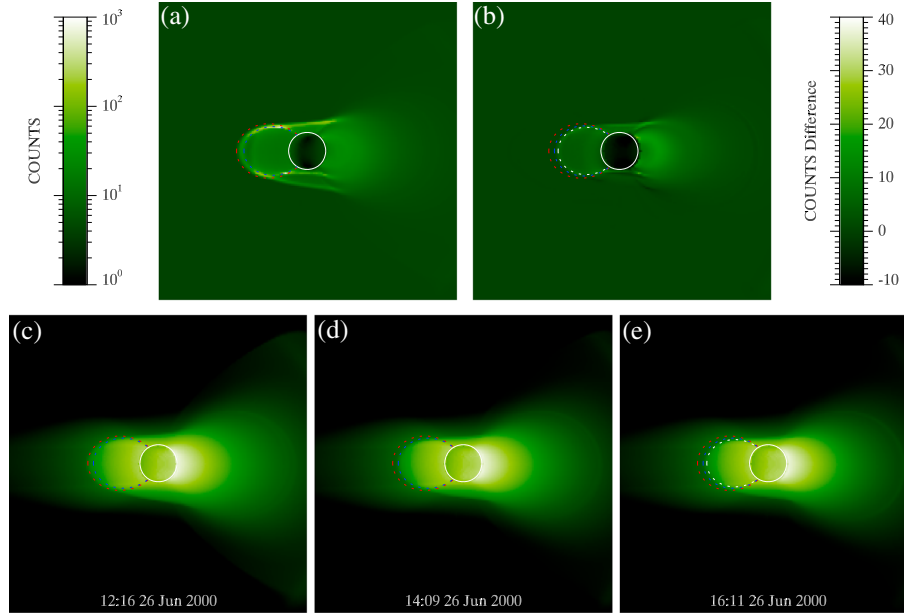
Figure 12. (a–b) Intensity changes of (c–e) EUV images detected at position f at three UTs for storm on 26 June 2000. Dashed red lines represent the dipole field lines with L value of 3.8. Dashed blue lines represent the dipole field lines with L value of 3.5. Dashed white lines represent the dipole field lines with L value of 3.3. Solid white circles represent the Earth. The log-scaled color bar at left represents the instrument counts. (a) is obtained by subtracting (d) from (c) while (b) is obtained by subtracting (e) from (d). The linear-scaled color bar at right represents the count differences between adjacent images.

[46] 3. Directions and shapes of the plumes change dramatically with imaging positions for the moon-based images. For example,

    a. The plumes might be at center of the images and extend along the vertical direction (see Figures 9b, 9c, 10h, and 11i), and then, the longitudinal direction of plumes on the equatorial plane might be parallel to the axis of the FOV of the imager. If the plumes in the EUV images have no wrapping, the plumes on the equatorial plane will extend directly in vertical direction from the main plasmasphere.

    b. The plumes might be at the right (Figures 9d, 10e, and 10f) or left edge (Figures 11j–11l) of the images and attached to the main body of the plasmasphere with a diffusive distribution, and then, the direction of plumes on the equatorial plane might be perpendicular to the axis of the FOV of the imager.

    c. The plumes might be at the right (Figure 6) or left (Figures 7g, 7h, 8i, and 8j) edge of the images and encircle the main body of the plasmasphere, and then, the plumes might be wrapped on the equatorial plane.

    d. The plumes might move from left to right (Figure 9c) or from right to left (Figure 11i) in the images, revealing that the plumes are rotating duskward on the equatorial plane.

Above analysis of the relations between the LOS and the locations of the structures has been confirmed by SELENE observations [*Murakami et al.*, 2013]. When the plasmaspheric filament structures in *Murakami et al.* [2013, Figures 2 and 3] are traced onto the SM equatorial plane using the Minimum L Algorithm [*Wang et al.*, 2007; *He et al.*, 2012], the positions

for the two cases are (3.7 R_E, 06:58 MLT) and (3.5 R_E, 08:20 MLT), respectively, in consistent with Murakami et al. results. The positions of the moon at 09:30 UT on 2 June 2008 (10:30 MLT in SM) and at 07:00 UT on 8 May 2008 (14:38 MLT in SM) are once known; the positions of the filaments around the Earth's dawn sector can be directly deduced without line tracing.

[47] 4. Erosions of the plasmasphere from the moon-based imaging are different from the polar orbit imaging. The first difference is the erosion of the main body of the plasmasphere. In polar orbit images, the erosion of the main body of the plasmasphere is more or less like a circle shrinking toward its center [*Goldstein et al.*, 2003; *Spasojević et al.*, 2003], whereas in the moon-based images, the low-latitude parts of the images erode more sharply than the high-latitude parts of the images (e.g., Figures 9c and 11i). The second difference is the erosion of the plume. Take unwrapped plume, for example, its erosion appears as narrowing in longitudinal direction and rotating toward dusk as seen by IMAGE in Figure 1d–1f, whereas the plume becomes narrow in horizontal direction and shifts horizontally in the moon-based images in Figures 9b, 9c, 10h, and 11i.

[48] 5. Boundary motion and local number density of the plumes may be reconstructed. From a single moon-based EUV image, the shape (or boundary) of the shoulder and the plume can be deduced through the image reconstruction algorithm, which can be found in *He et al.* [2011], and from a series of images, the boundary motions and the local number density changes can be obtained then. It is demonstrated in *He et al.* [2011, Figure 10 and equation 6] that the density profile in the plume may follow the same logarithmic law as the density profile in the main plasmasphere. Together with the upcoming Wide-Angle Auroral Imager on board the
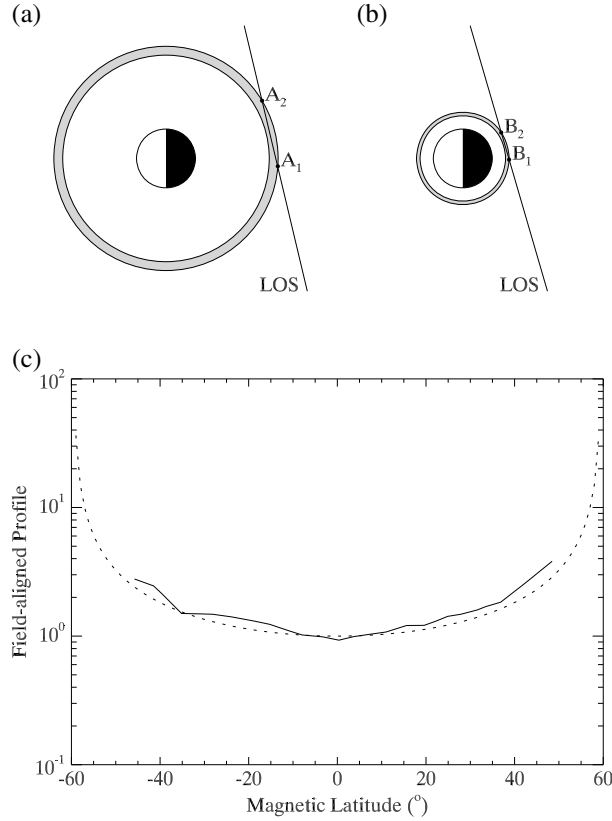
Figure 13. Diagram for the calculation of the effective length of LOS in field-aligned profile extraction for the (a) equatorial plane and (b) magnetic latitude of 50°. Both are the polar views. The gray rings represent the eroded parts of the plasmasphere. The outer and inner radii of the ring in Figure 13a are 3.8 R_E and 3.5 R_E, respectively, while in Figure 13b, these values are 1.6 R_E and 1.5 R_E, respectively. (c) Field-aligned profiles are obtained by dividing the density by the equatorial plane density. The solid line is obtained by the method explained in the text. The dashed line is $N_e(\lambda)/N_0$ ($L = 3.6$) in formula 4.

Chinese FengYun-3 (FY-3) satellite which will image the N_2 Lyman-Birge-Hopfield bands to get the global pictures of the aurora and the ionosphere, we can investigate the coupling of the plumes to the ionosphere and the ionospheric signatures of the plumes. Furthermore, knowing the boundaries of the plumes, the effect of the SW/magnetosphere coupling on the plumes can also be investigated [*Borovsky and Denton*, 2006].

[49] 6. Latitudinal information of the magnetic flux tubes may be deduced from adjacent moon-based images since the background intensity outside the plasmapause does not change much in a short period (10 min). Take Figure 12 for an example. From the three adjacent EUV images detected at position *f*, if the plasmasphere is refilled or eroded, then the number of magnetic flux tubes will increase or decrease. From 12:16 UT to 16:11 UT, the plasmasphere is eroded, and the outmost magnetic flux tube on this meridian is removed from the main body of the plasmasphere in Figures 12c–12e.

[50] It is clearly shown from Figure 12a that the shape of the removed magnetic flux tube is approximately coincident

with the dipole field line with *L* values of 3.5–3.8 while the *L* values are 3.3–3.5 in Figure 12b. The inconsistencies at high latitudes might be caused by the angle between the projection plane and the SM meridian plane. The intensity changes in the region between the dipole field lines $L = 3.5$ and $L = 3.8$ in Figure 12a are converted to He$^+$ density, and the profile is presented in Figure 13c. When the plasmasphere is eroded from boundary $L = 3.8$ to boundary $L = 3.5$ as illustrated in Figure 13a, the intensity changes in Figure 12a are mostly contributed by the gray ring in Figure 13a, while the plasmaspheric trough outside the ring changes little during the erosion. Thus, only the gray ring region is considered in calculation of the length of LOS with the method adopted in previous studies [*Gallagher et al.*, 2005; *Murakami et al.*, 2013]. At equatorial plane, this length (A$_1$A$_2$ in Figure 13a) is ∼ 2.4 R_E and reduces to ∼1.0 R_E at the latitude of 50° (B$_1$B$_2$ in Figure 13b) in the dipole field. By assuming the densities to be constants along the LOS in the gray ring, the He$^+$ density can be calculated by equation 5. The latitudinal profile of the calculated density is in agreement with Tu et al. model adopted in this study as shown in Figure 13c. The difference at midlatitudes might be because of the underestimating of the length of the LOS. It is illustrated from the results in Figure 13c that the latitudinal distribution of the plasmasphere can be estimated from the intensity changes in adjacent EUV images.

4.3. Plasmaspheric Response to SW-IMF

[51] It is revealed from IMAGE observations that the SW-IMF greatly affects and controls the global structures and dynamic evolutions of the plasmasphere, even though there are limited cases available for investigating this issue due to the observation limitations of the IMAGE EUV on the global structures of the plasmasphere [e.g., *Goldstein et al.*, 2002; *Spasojević et al.*, 2003; *Gallagher et al.*, 2005]. CE-3 provides the best platform to address this problem. As cited above, the continuous observing period of CE-3 can reach ∼12 days, and more storms might be caught to investigate the plasmaspheric responses to the SW-IMF. The relationship between the plasmaspheric configurations and the SW-IMF conditions might be easily assessed in future.

4.4. Erosion and Refilling of Plasmasphere

[52] As discussed in section 4.2, the latitudinal information of specific magnetic flux tube can be extracted from moon-based EUV images, and the shape, the boundary motions, and the local number density changes of the plume can be obtained from a series of images by using the image reconstruction algorithm proposed by *He et al.* [2011]. It is expected to study how a magnetic flux tube is connected with ionosphere with high density during refilling/erosion events and how the equilibrium is established in the process of refilling/erosion. Furthermore, since the FOV of CE-3 EUV is 15°, the boundary of the plume can be traced to as far as the magnetopause, and the coupling of the plume to the magnetopause especially at the dayside reconnection site and the plasma loss to the magnetopause can be studied to further understand the coupling between the SW-IMF and the magnetosphere.

5. Summary

[53] The CE-3 EUV imager will provide us with a unique opportunity to study the global dynamics of the plasmasphere. In order to better understand global structures and dynamics of the plasmasphere in a new perspective, the radiation intensities, global structures, and temporal evolutions of the plasmasphere viewed from the moon are systematically simulated with the dynamic model of DGCPM, based on two typical storms observed by IMAGE EUV. The results are summarized as follows:

[54] 1. The 30.4 nm radiation intensity of the plasmasphere detected from the moon is $0.1 \sim 12.3$ R within the plasmapause and $0.02 \sim 0.1$ R outside the plasmapause. These values are larger than those detected from the polar orbit because both the column integrations range from the moon and the phase function are larger than those from the polar orbit. The intensities of the SWCX generated 30.4 nm emission and the geocoronal 58.4 nm emission, and their effects on the moon-based imaging will be investigated in future work.

[55] 2. Simulated EUV images exhibit new characteristics which can help us study the large-scale structures of the plasmasphere. The main body of the plasmasphere is approximately oval shaped, the plasmaspheric shoulder has two types of shapes (step shape and meniscus shape) according to different lunar positions, and the plasmaspheric plumes have different shapes under different SW-IMF conditions and different lunar positions. More storms will be identified in future moon-based imaging to investigate the responses of the plasmasphere to SW-IMF and geomagnetic conditions.

[56] 3. The evolutions of the plasmaspheric structures display new patterns in the moon-based EUV images, and the latitudinal information of specific magnetic flux tube can be extracted from the moon-based EUV images. It is found that the low-latitude part of the image erodes more sharply than the high-latitude part, the step-shape shoulder moves almost horizontally toward the center of the moon-based images, and the plume narrows and shifts in horizontal direction.

[57] 4. Based on IMAGE EUV observations that the typical scale sizes of plasmapause, shoulder, and plume are much larger than 0.1 R_E, and the average radial velocity of the plasmasphere during erosion or refilling in storm time is approximately 0.1 R_E/10 min [*Goldstein et al.*, 2003; *Murakami et al.*, 2007], it is expected that the CE-3 EUV with FOV of 15°, angular resolution of 0.095° (spatial resolution of 0.1 R_E), temporal resolution of 10 min, sensitivity of 0.12 count $R^{-1} s^{-1}$ pixel^{-1}, and sensitivity threshold of ~0.1 count min^{-1} pixel^{-1} will successfully image the plasmasphere so as to clearly identify the global structures of the plasmasphere.

[58] This investigation provides us with a clear overall understanding of the moon-based EUV imaging. The simulated results can help us to study the plasmaspheric structures in future moon-based EUV images and be used to perform image inversions in future work. It is expected that the plasmaspheric features simulated in this work will be identified in the observations of CE-3 EUV.

References

Adrian, M. L., D. L. Gallagher, J. L. Green, and B. R. Sandel (2001), The large-scale plasmaspheric density trough associated with the 24 May 2000 geomagnetic storm: IMAGE EUV observations and global core plasma modeling, *Eos Trans. AGU*, *82*, S352.

Borovsky, J. E., and M. H. Denton (2006), Effect of plasmaspheric drainage plumes on solar-wind/magnetosphere coupling, *Geophys. Res. Lett.*, *33*, L20101, doi:10.1029/2006GL026519.

Brandt, J. C. (1961), Interplanetary Gas, VI, on diffuse extreme ultraviolet helium radiation in the night and day sky, *Astrophys. J.*, *134*(2), 975–980.

Brandt, J. C., and J. W. Chamberlain (1959), Interplanetary Gas, I, hydrogen radiation in the night sky, *Astrophys. J.*, *130*(1), 670–682.

Burch, J. L. (2000), IMAGE mission overview, *Space Sci. Rev.*, *91*(1), 1–14.

Carpenter, D. L. (2004), Remote sensing the Earth's plasmasphere, *Rad. Sci. Bull.*, *308*, 13–29.

Carpenter, D. L., and R. R. Anderson (1992), An ISEE/Whistler model of equatorial electron density in the magnetosphere, *J. Geophys. Res.*, *97*(A2), 1097–1108.

Chen, A. J., and R. A. Wolf (1972), Effects on the plasmasphere of a time-varying convection electric field, *Planet. Space Sci.*, *20*(4), 483–509.

Craven, P. D., D. L. Gallagher, and R. H. Comfort (1997), Relative concentration of He$^+$ in the inner magnetosphere as observed by the DE 1 retarding ion mass spectrometer, *J. Geophys. Res.*, *102*(A2), 2279–2289.

Denton, R. E., M. F. Thomsen, K. Takahashi, R. R. Anderson, and H. J. Singer (2011), Solar cycle dependence of bulk ion composition at geosynchronous orbit, *J. Geophys. Res.*, *116*, A03212, doi:10.1029/2010JA016027.

Gallagher, D. L., P. D. Craven, and R. H. Comfort (2000), Global core plasma model, *J. Geophys. Res.*, *105*(A8), 18,819–18,833.

Gallagher, D. L., M. L. Adrian, and M. W. Liemohn (2005), Origin and evolution of deep plasmaspheric notches, *J. Geophys. Res.*, *110*, A09201, doi:10.1029/2004JA010906.

Garrido, D. E., R. W. Smith, D. W. Swift, S.-I. Akasofu, R. M. Robinson, and Y. T. Chiu (1994), Imaging the plasmasphere and trough regions in the extreme ultraviolet region, *Opt. Eng.*, *33*(2), 371–382.

Goldstein, J., R. W. Spiro, P. H. Reiff, R. A. Wolf, B. R. Sandel, J. W. Freeman, and R. L. Lambour (2002), IMF-driven overshielding electric field and the origin of the plasmaspheric shoulder of May 24 2000, *Geophys. Res. Lett.*, *29*(16), doi:10.1029/2001GL014534.

Goldstein, J., B. R. Sandel, W. T. Forrester, and P. H. Reiff (2003), IMF-driven plasmasphere erosion of 10 July 2000, *Geophys. Res. Lett.*, *30*(3), 1146, doi:10.1029/2002GL016478.

Gruntman, M. (1992), Charge-exchange born He$^+$ ions in the solar wind, *Geophys. Res. Lett.*, *19*, 1323–1326.

Gruntman, M. (2001), Imaging the three-dimensional solar wind, *J. Geophys. Res.*, *106*(A5), 8205–8216.

Gruntman, M., V. Izmodenov, and V. Pizzo (2006), Imaging the global solar wind flow in EUV, *J. Geophys. Res.*, *111*, A04216, doi:10.1029/2005JA011530.

He, F., B. Chen, and X. X. Zhang (2010a), Moon-based imaging of the Earth's plasmaspheric extreme ultraviolet radiation, *Opt. Prec. Eng.*, *18*(12), 2564–2573 (in Chinese).

He, F., X. X. Zhang, B. Chen, and M.-C. Fok (2010b), Calculation of the extreme ultraviolet radiation of the Earth's plasmasphere, *Sci. China Tech. Sci.*, *53*(1), 200–205.

He, F., X. X. Zhang, B. Chen, and M.-C. Fok (2011), Reconstruction of the plasmasphere from moon-based EUV images, *J. Geophys. Res.*, *116*, A11203, doi:10.1029/2010JA016364.

He, F., X. X. Zhang, B. Chen, and M.-C. Fok (2012), Plasmaspheric trough evolution under different conditions of subauroral ion drift, *Sci. China Tech. Sci.*, *55*, 1–8, doi:10.1007/s11431-012-4781-1.

Jelinsky, P., J. V. Vallerga, and J. Edelstein (1995), First spectral observations of the diffuse background with the Extreme Ultraviolet Explorer, *Astrophys. J.*, *442*(4), 653–661.

Lemaire, J. F., and K. I. Gringauz (1998), *The Earth's Plasmasphere*, Cambridge Univ. Press, New York.

Lennartsson, W., and R. D. Sharp (1982), A comparison of the 0.1–17 keV/e ion composition in the near equatorial magnetosphere between quiet and

disturbed conditions, *J. Geophys. Res.*, *87*(A8), 6109–6120, doi:10.1029/JA087iA08p06109.

Liemohn, M. W., A. J. Ridley, D. L. Gallagher, D. M. Ober, and J. U. Kozyra (2004), Dependence of plasmaspheric morphology on the electric field description during the recovery phase of the 17 April 2002 magnetic storm, *J. Geophys. Res.*, *109*, A03209, doi:10.1029/2003JA010304.

Liemohn, M. W., A. J. Ridley, J. U. Kozyra, D. L. Gallagher, M. F. Thomsen, M. G. Henderson, M. H. Denton, P. C. Brandt, and J. Goldstein (2006), Analyzing electric field morphology through data-model comparisons of the Geospace Environment Modeling Inner Magnetosphere/Storm Assessment Challenge events, *J. Geophys. Res.*, *111*, A11S11, doi:10.1029/2006JA011700.

Matsui, H., T. Mukai, S. Ohtani, K. Hayashi, and R. C. Elphic (1999), Cold dense plasma in the outer magnetosphere, *J. Geophys. Res.*, *104*(A11), 25,077–25,095.

Meier, R. R. (1991), Ultraviolet spectroscopy and remote sensing of the upper atmosphere, *Space Sci. Rev.*, *58*(1), 1–185.

Meier, R. R., and C. S. Weller (1972), EUV resonance radiation from helium atoms and ions in the geocorona, *J. Geophys. Res.*, *77*(7), 1190–1204.

Murakami, G., M. Hirai, and I. Yoshikawa (2007), The plasmapause response to the southward turning of the IMF derived from sequential EUV images, *J. Geophys. Res.*, *112*, A06217, doi:10.1029/2006JA012174.

Murakami, G., I. Yoshikawa, K. Yoshioka, A. Yamazaki, M. Kagitani, M. Taguchi, M. Kikuchi, S. Kameda, and M. Nakamura (2013), Plasmaspheric filament: An isolated magnetic flux tube filled with dense plasmas, *Geophys. Res. Lett.*, *40*, 250–254, doi:10.1002/grl.50124.

Nakamura, M., et al. (1999), Helium observation in the Martian ionosphere by an X-ray ultraviolet scanner on Mars orbiter NOZOMI, *Earth Planets Space*, *51*, 61–70.

Nakamura, M., I. Yoshikawa, A. Yamazaki, K. Shiomi, Y. Takizawa, M. Hirahara, K. Yamashita, Y. Saito, and W. Miyake (2000), Terrestrial plasmaspheric imaging by an Extreme Ultraviolet Scanner on Planet-B, *Geophys. Res. Lett.*, *27*(2), 141–144.

Ober, D. M., J. L. Horwitz, and D. L. Gallagher (1997), Formation of density troughs embedded in the outer plasmasphere by subauroral ion drift events, *J. Geophys. Res.*, *102*(A7), 595–602.

Ober, D. M., J. L. Horwitz, and D. L. Gallagher (1998), Convection of plasmaspheric plasma into the outer magnetosphere and boundary layer region: Initial results, in *Geospace Mass and Energy Flow: Results From the ISTP Program*, Geophys. Monogr. Ser., vol. 104, edited by J. L. Horwitz, D. L. Gallagher, and W. K. Peterson, pp. 45–51, AGU, Washington, D.C.

Ogawa, T., and T. Tohmatsu (1971), Sounding rocket observation of helium 304- and 584-A glow, *J. Geophys. Res.*, *76*(25), 6136–6145.

Paresce, F., S. Bowyer, and S. Kumar (1973), Observations of the He II 304-A radiation in the night sky, *J. Geophys. Res.*, *78*(1), 71–79.

Paresce, F., H. Fahr, and G. Lay (1981), A search for interplanetary He II 304-A emission, *J. Geophys. Res.*, *86*(A12), 10,038–10,048.

Paschmann, G., N. Sckopke, G. Haerendel, J. Papamastorakis, S. J. Bame, J. R. Asbridge, J. T. Gosling, E. W. Hones Jr., and E. R. Tech (1978), ISEE plasma observations near the subsolar magnetopause, *Space Sci. Rev.*, *22*, 717–737.

Rasmussen, C. E., S. M. Guitar, and S. G. Thomas (1993), A two-dimensional model of the plasmasphere: Refilling time constant, *Planet. Space Sci.*, *41*(1), 35–43.

Roelof, E. C., and A. J. Skinner (2000), Extraction of ion distributions from magnetospheric ENA and EUV images, *Space Sci. Rev.*, *91*, 437–459.

Roelof, E. C., B. H. Mauk, and R. R. Meier (1992), Instrument requirements for imaging the magnetosphere in extreme ultraviolet and energetic neutral atoms derived from computer-simulated images, *Proc. SPIE*, *1744*, 19–30.

Sandel, B. R., et al. (2000), The extreme ultraviolet imager investigation for the image mission, *Space Sci. Rev.*, *91*(1), 197–242.

Sandel, B. R., R. A. King, W. T. Forrester, D. L. Gallagher, A. L. Broadfoot, and C. C. Curtis (2001), Initial results from the IMAGE Extreme Ultraviolet Imager, *Geophys. Res. Lett.*, *28*(8), 1439–1442.

Sandel, B. R., J. Goldstein, D. L. Gallagher, and M. Spasojević (2003), Extreme ultraviolet imager observations of the structure and dynamics of the plasmasphere, *Space Sci. Rev.*, *109*(1), 25–46.

Sasaki, S., Y. Iijima, K. Tanaka, M. Kato, M. Hashimoto, H. Mizutani, and Y. Takizawa (2003), The SELENE mission: Goals and status, *Adv. Space Res.*, *31*(11), 2335–2340.

Sitnov, M. I., N. A. Tsyganenko, A. Y. Ukhorskiy, and P. C. Brandt (2008), Dynamical data-based modeling of the storm-time geomagnetic field with enhanced spatial resolution, *J. Geophys. Res.*, *113*, A07218, doi:10.1029/2007JA013003.

Spasojević, M., J. Goldstein, D. L. Carpenter, U. S. Inan, B. R. Sandel, M. B. Moldwin, and B. W. Reinisch (2003), Global response of the plasmasphere to a geomagnetic disturbance, *J. Geophys. Res.*, *108*(A9), 1340, doi:10.1029/2003JA009987.

Swift, D. W., R. W. Smith, and S.-I. Akasofu (1989), Imaging the Earth's magnetosphere, *Planet. Space Sci.*, *37*(4), 379–384.

Tsyganenko, N. A., and M. I. Sitnov (2007), Magnetospheric configurations from a high-resolution data-based magnetic field model, *J. Geophys. Res.*, *112*, A06225, doi:10.1029/2007JA012260.

Tu, J.-N., P. Song, B. W. Reinisch, J. L. Green, and X.-Q. Huang (2006), Empirical specification of field-aligned plasma density profiles for plasmasphere refilling, *J. Geophys. Res.*, *111*, A06216, doi:10.1029/2005JA011582.

Wang, C., T. S. Newman, and D. L. Gallagher (2007), Plasmapause equatorial shape determination via the Minimum L Algorithm: Description and evaluation, *J. Geophys. Res.*, *112*, A12201, doi:10.1029/2006JA012202.

Weimer, D. R. (2005), Improved ionospheric electrodynamic models and application to calculating Joule heating rates, *J. Geophys. Res.*, *110*, A05306, doi:10.1029/2004JA010884.

Wu, F. M., K. Suzuki, R. W. Carlson, and D. L. Judge (1981), PIONEER 10 ultraviolet photometer observations of the interplanetary glow at heliocentric distances from 2 to 14 AU, *Astrophys. J.*, *245*(5), 1145–1158.

Yoshikawa, I., A. Yamazaki, K. Shiomi, K. Yamashita, Y. Takizawa, and M. Nakamura (2001), Loss of plasmaspheric ions during a storm observed by the EUV scanner onboard Planet-B, *J. Geophys. Res.*, *106*(A9), 18,911–18,918.

Yoshikawa, I., et al. (2008), Telescope of extreme ultraviolet (TEX) onboard SELENE: Science from the Moon, *Earth Planets Space*, *60*(4), 407–416.